UCSF

Title

Translation control of the immune checkpoint in cancer and its therapeutic targeting

Permalink

Journal

ISSN

Authors

Xu, Yichen
Poggio, Mauro
Jin, Hyun Yong
et al.

Publication Date

DOI

Peer reviewed

Translation control of the immune checkpoint in cancer and its therapeutic targeting

Yichen Xu[1,2,11], **Mauro Poggio**[1,2,11], **Hyun Yong Jin**[1,2], **Zhen Shi**[3,4], **Craig M. Forester**[1,2,5], **Ying Wang**[1,2,6], **Craig R. Stumpf**[1,2,7], **Lingru Xue**[1,2], **Emily Devericks**[1,2], **Lomon So**[1,2], **Hao G. Nguyen**[1,2], **Alice Griselin**[1,2], **John D. Gordan**[2], **Sarah E Umetsu**[8], **Siegfried H. Reich**[7], **Stephen T. Worland**[7], **Saurabh Asthana**[2], **Maria Barna**[3,4], **Kevin R. Webster**[7], **John T. Cunningham**[1,2,9], and **Davide Ruggero**[1,2,10,★]

[1]Department of Urology, University of California, San Francisco, San Francisco, CA, USA.

[2]Helen Diller Family Comprehensive Cancer Center, University of California, San Francisco, San Francisco, CA, USA.

[3]Department of Developmental Biology, Stanford University, Stanford, CA, USA.

[4]Department of Genetics, Stanford University, Stanford, CA, USA.

[5]Division of Pediatric Allergy, Immunology & Bone Marrow Transplantation, University of California, San Francisco, San Francisco, CA, USA.

[6]State Key Laboratory of Pharmaceutical Biotechnology, Nanjing Advanced Institute for Life Sciences, School of Life Sciences, Nanjing University, Nanjing, Jiangsu, China.

[7]eFFECTOR Therapeutics, San Diego, CA, USA.

[8]Department of Pathology, University of California, San Francisco, San Francisco, CA, USA.

[9]Department of Cancer Biology, University of Cincinnati College of Medicine, Cincinnati, OH, USA.

[10]Department of Cellular and Molecular Pharmacology, University of California, San Francisco, San Francisco, CA, USA.

[11]These authors contributed equally: Yichen Xu, Mauro Poggio.

Abstract

Cancer cells develop mechanisms to escape immunosurveillance, among which modulating the expression of immune suppressive messenger RNAs is most well-documented. However, how this is molecularly achieved remains largely unresolved. Here, we develop an in vivo mouse model of liver cancer to study oncogene cooperation in immunosurveillance. We show that MYC overexpression (MYC^{Tg}) synergizes with $KRAS^{G12D}$ to induce an aggressive liver tumor leading to metastasis formation and reduced mouse survival compared with $KRAS^{G12D}$ alone. Genome-wide ribosomal footprinting of $MYC^{Tg};KRAS^{G12}$ tumors compared with $KRAS^{G12D}$ revealed potential alterations in translation of mRNAs, including programmed-death-ligand 1 (PD-L1). Further analysis revealed that PD-L1 translation is repressed in $KRAS^{G12D}$ tumors by functional, non-canonical upstream open reading frames in its 5′ untranslated region, which is bypassed in $MYC^{Tg};KRAS^{G12D}$ tumors to evade immune attack. We show that this mechanism of PD-L1 translational upregulation was effectively targeted by a potent, clinical compound that inhibits eIF4E phosphorylation, eFT508, which reverses the aggressive and metastatic characteristics of $MYC^{T9};KRAS^{G12D}$ tumors. Together, these studies reveal how immune-checkpoint proteins are manipulated by distinct oncogenes at the level of mRNA translation, which can be exploited for new immunotherapies.

Reporting Summary.

Further information on experimental design is available in the Nature Research Reporting Summary linked to this article.

The concept that the immune system can control tumor growth can be traced back to 1893 when William Coley used live bacteria as an immune stimulant to treat cancer. This natural protective mechanism of the human body to control cancer is now known to be elicited by key immune-checkpoint molecules, often present on cytotoxic T cells[1]. However, tumor cells can exploit these immune-checkpoint pathways as a mechanism to evade detection by the immune response, for example by altering the expression of key ligands on tumor cells such as PD-L1 and CD80/86, to inhibit the cytotoxicity activity of immune cells. Understanding the underlying mechanism by which cancer cells can 'molecularly cloak' themselves and remain hidden to immune surveillance is of great interest to cancer biology and provides the rationale design of therapeutic interventions. Although direct transcriptional control of inhibitory immune-checkpoint molecules by specific oncogenic pathways has been reported[2,3], post-transcriptional control may offer a fast, highly tunable mechanism to control the abundance of effector proteins guiding immune evasion of cancer cells. Yet, this level of regulation of the immune-checkpoint molecules remains largely uncharacterized.

To study how oncogene cooperation directs immune-checkpoint deregulation, we focused on primary liver cancer, the second leading cause of cancer deaths worldwide[4]. Hepatocellular

carcinoma (HCC) lacks effective cures except for early surgical intervention or liver transplantation, highlighting the urgent need for new therapeutic strategies. *c-MYC,* overexpression of which is commonly caused by genomic amplification, is widely amplified[5] and present in 70% of viral and alcohol-related HCC[6] and has a critical role in the malignant transformation of hepatocytes into HCC[7,8]. Of all genetic alternations in HCC patients, there is an over-representation of pathways related to receptor tyrosine kinase (RTK) signaling, with ~22–37% of HCC patients having at least one alternation in genes associated to RTK/RAS/PI3K pathway[5]. Here, we discovered that *MYC*, when cooperating with RTK/RAS signaling, markedly increases HCC formation and metastasis development. We further characterize the importance of evasion from immune attack as a key driver of primary and metastatic cancer development and define an unexpected post-transcriptional control of gene expression that drives this process. We also show that a potent clinical compound inhibiting the phosphorylation of the major cap-binding protein, eIF4E, can restore cancer immunosurveillance.

Results

MYC and *KRAS* cooperate in inducing liver cancer with metastatic potential and an altered immune microenvironment.

We developed a genetic engineered mouse (GEM) model of liver cancer with enhanced MYC and RTK signaling. We first generated an HA-tagged, *c-MYC* transgene, whereby GFP is co-translated via a viral internal ribosome entry site element that is driven in a CRE-dependent manner (referred to here as: MYC^{Tg}; Supplementary Fig. 1a–c).We then crossed this *c-MYC* transgenic mouse to a well-established Cre-inducible, constitutively active $KRAS^{G12D}$ mouse that mimics notably enhanced downstream signaling of RTK[9,10], whereby liver-specific expression is achieved through Albumin-Cre- mediated recombination (Supplementary Fig. 1d,e). In this setting, *MYC* overexpression in the liver was not sufficient to drive cancer in vivo, whereas $KRAS^{G12D}$ and *MYC* (referred to here as MYC^{Tg};$KRAS^{G12D}$) synergized to provoke a more aggressive tumor compared with the $KRAS^{G12D}$ alone (Fig. 1a). This aggressive tumor was characterized by decreased tumor latency (Fig. 1a), the simultaneous presence of intrahepatic cholangiocarcinoma and HCC (Fig. 1b), as well as decreased survival. Notably, MYC^{Tg};$KRAS^{G12D}$ mice showed a marked increase in metastasis in 90% of animals, compared with only 10% in $KRAS^{G12D}$ alone (Fig. 1c,d). Metastasis occurred primarily in the lungs (Fig. 1d), but could also be identified in lymph nodes (Supplementary Fig. 1f). These findings suggest that the barrier for primary and metastatic tumor development in $KRAS^{G12D}$ tumors is broken by *MYC* hyperactivation.

By characterizing the microenvironment of MYC^{Tg};$KRAS^{G12D}$ tumors, we observed a robust invasion of inflammatory cells in comparison to $KRAS^{G12D}$ alone (Fig. 1e). Notably, MYC^{Tg};$KRAS^{G12D}$-driven inflammatory cell infiltration is characterized by increased CD45+ leukocytes including neutrophils and macrophages (Fig. 1f and Supplementary Fig. 1g–i). The infiltration of inflammatory cells has been shown to enhance tumor angiogenesis, proliferation, metastasis, and therapy resistance[11], and therefore may contribute to the aggressive phenotype of MYC^{Tg};$KRAS^{G12D}$-driven cancer. Notably, we also detected an increased infiltration of a cytotoxic, CD8+ T cell biased tumor-infiltrating lymphocytes (Fig.

1g and Supplementary Fig. 1j), which has a central role in anti-tumor immunity and tumor regression. However, despite the increased CD8+ T cell population that has been associated with an improved prognosis[12–14], MYC^{Tg};$KRAS^{G12D}$-driven liver cancer progresses more aggressively. Based on these, we proposed that cancer cells with MYC and $KRAS$ activation may escape immune surveillance and suppress the cytotoxicity of CD8+ T cells in the tumor microenvironment[15–18]. This escape from immune surveillance may be a broader characteristic of MYC and $KRAS$-driven cancers[19].

MYC and *KRAS* cooperation selectively alters gene expression at the translation level.

We proposed that MYC and $KRAS$ cooperate to drive unique gene expression programs in cancer cells to evade immune-destruction and develop metastasis. To survey the genome-wide gene expression at both the transcription and translation level in an unbiased manner, we first carefully micro-dissected primary liver tumor nodules in MYC^{Tg};$KRAS^{G12D}$ and $KRAS^{G12D}$ mice as well as wild-type livers as controls. We deep-sequenced total mRNAs and ribosome-protected mRNA fragments using ribosome profiling[20] to generate genome-wide transcriptional and translational landscapes, respectively (Supplementary Fig. 2). Applying the framework of the generalized linear model, a linear regression was performed to the normalized read counts, as a function of sample type variables ('WT', '$KRAS^{G12D}$', or 'MYC^{Tg};$KRAS^{G12D}$'). Here, the coefficient of sample type variables (that is, 'MYC^{Tg};$KRAS^{G12D}$' over '$KRAS^{G12D}$') is a measurement of corresponding differential gene expression. The transcriptional expression profile in the MYC^{Tg};$KRAS^{G12D}$ murine model of HCC exhibits significant similarities to human HCC (Supplementary Fig. 3). Human HCC samples harboring both MYC amplification and RTK signaling activation (Supplementary Fig. 3a) possess a gene expression pattern that strongly correlated with that of our MYC^{Tg};$KRAS^{G12D}$ murine HCC (Supplementary Fig. 3b,c). These findings support that our GEM model is a highly relevant and suitable model for studying human HCC. When the global transcriptome (RNA-Seq) and translatome (Ribo-Seq) profiles were directly compared, we observed that activation of $KRAS$ alone results in a coordinated change in RNA-Seq and Ribo-seq compared with wild-type hepatocytes (Fig. 2a, Supplementary Fig. 4, and Supplementary Table 1). In the context of both MYC and $KRAS$ activation, we detected few statistically significant changes at the mRNA level compared with $KRAS$ activation alone (11 down- and 13 upregulated transcripts with $P_{adj} < 0.1$ and |$\log_2$FC| > 2 in RNA-Seq) (Fig. 2a and Supplementary Table 2), but we observed changes in ribosome footprints for a subset of transcripts (130 down- and 339 upregulated transcripts with $P_{adj} < 0.1$ and |$\log_2$FC| > 2 in Ribo-Seq) (Fig. 2a, Supplementary Fig. 4, and Supplementary Table 2). Further validation will be required to determine whether these Ribo-Seq changes are a result of a combination of changes in transcription and translation or translation/transcription alone (Supplementary Fig. 4). Nevertheless, these findings raise the possibility that in the context of two cooperating oncogenes, the translational profile of gene expression is distinct.

MYC reprograms PD-L1 expression at the translation level.

To further investigate possible translational regulation in MYC^{Tg};$KRAS^{G12D}$ tumors, we first performed gene ontology analysis on the 339 transcripts with significantly upregulated ribosome footprints in MYC^{Tg};$KRAS^{G12D}$ tumors compared with $KRAS^{G12D}$ ($P_{adj} < 0.1$

and $\log_2 FC > 2$ in Ribo-Seq). This revealed several significantly enriched gene ontology categories ($P_{adj} < 0.05$) that were grouped into major functional clusters including: defense response, cell activation, chemotaxis, cell cycle process, and cellular response to chemical stimulus (Fig. 2b and Supplementary Table 3). Notably, in the cell activation cluster, we found the immune-checkpoint gene *Cd274* encoding the mouse ortholog of PD-L1 (Fig. 2b and Supplementary Fig. 5). Despite PD-L1 mRNA being relatively equally induced in both *KRAS*[G12D] and *MYC*[Tg];*KRAS*[G12D] tumors, PD-L1 ribosome foot-prints are notably upregulated in *MYC*[Tg];*KRAS*[G12D] (Supplementary Table 2), suggesting possible translational upregulation of the gene. PD-L1 is a transmembrane protein expressed on tumor cells that is a ligand of the immune-checkpoint receptor programmed death-1 (PD-1) on T cells. PD-L1/PD-1 interaction leads to the negative regulation of T cell proliferation, migration and activation, allowing tumor cells to evade the anti-tumor immune response[21], which matches the phenotype of the *MYC*[Tg];*KRAS*[G12D] tumor. Thus, we suggested that the translational upregulation of PD-L1 by MYC and RAS cooperation may lead to immune evasion and the aggressive cancer phenotype in *MYC*[Tg];*KRAS*[G12D] mice. As PD-L1 is also widely expressed on tumor-infiltrating immune cells such as T cells and some myeloid cells[22,23], we first confirmed HCC tumor-specific expression of PD-L1 using immunofluorescence-based co-staining of *MYC*[Tg]-expressing liver cells with PD-L1 (Fig. 2c). Consistent with our ribosome-profiling analysis showing an approximate fivefold increase in ribosome footprints at the PD-L1 mRNA in *MYC*[Tg];*KRAS*[G12D] compared with *KRAS*[G12D] (Supplementary Fig. 5), there is a corresponding fourfold increase of PD-L1 protein abundance observed in *MYC*[Tg];*KRAS*[G12D] tumors by immunofluorescence (Fig. 2c), and this occurred independently of changes in mRNA amounts (Fig. 2d).

To validate that PD-L1 is regulated at the translation level in *MYC*[Tg];*KRAS*[G12D] liver cancer cells, we derived ex vivo cultures of primary, single-clone cell lines from individual liver tumors from *KRAS*[G12D] or *MYC*[Tg];*KRAS*[G12D] mice (Supplementary Fig. 6a–c). Noteworthy and consistent with previous studies, PD-L1 protein expression is typically assessed by flow cytometry[24–27]. Using the in vitro culturing of these cell lines, we specifically observed an increase in protein abundance of PD-L1 by flow cytometry in the *MYC*[Tg];*KRAS*[G12D] background with no significant difference at the mRNA level (Fig. 2e and Supplementary Fig. 6d), which also demonstrates that the upregulation of PD-L1 in *MYC*[Tg];*KRAS*[G12D] tumor is a result of primary oncogenic cooperation, rather than a reaction to anti-tumor immunity from the tumor microenvironment.Besides PD-L1, we also validated other translationally regulated mRNAs identified by ribosome profiling in the *MYC*[Tg];*KRAS*[G12D] tumor setting. We confirmed that cytokines involved in immune cell attraction and inflammation (CCL2 and CXCL9), proteins involved in the cell cycle process (PLK1, CDC20), and proteins involved in cell motility (SNAIL and CXCR6) are also regulated by MYC at the protein level (Supplementary Fig. 6e–g) without affecting their mRNA expression (Supplementary Fig. 6h).

Although *MYC* itself is a regulator of global protein synthesis, no noticeable increase in global protein synthesis rates in *MYC*[Tg];*KRAS*[G12D] compared with *KRAS*[G12D] cells was evident (Fig. 2f). To further characterize translational control of the PD-L1 mRNA in *MYC*[Tg];*KRAS*[G12D] liver tumor cells, we examined its distribution in polysomes (translationally active ribosome fractions) on sucrose gradient fractionation (Fig. 2f). There

is a higher percentage of PD-L1 mRNA accumulated in the translationally inactive free subunit and monosome fractions (fractions 2–6) in $KRAS^{G12D}$ liver tumor cells (Fig. 2f and Supplementary Fig. 7a), revealing that the translation of PD-L1 mRNA is relatively suppressed in $KRAS^{G12D}$ cells. However, in $MYC^{Tg};KRAS^{G12D}$ cells there was a significant shift of PD-L1 mRNA, but not the GAPDH control mRNA, towards the translationally active, polysome fractions (fractions 8–11) (Fig. 2f and Supplementary Fig. 7a,b), showing that the control of PD-L1 expression is at the level of mRNA translation in MYC^{Tg} and $KRAS^{G12D}$ cooperation-driven cancer. This is consistent with the observation made in fresh frozen human HCC tumor samples (Supplementary Fig. 8a,b), where we observed a significant correlation between MYC amounts and PD-L1 protein abundances (Fig. 2g), whereas PD-L1 mRNA expression was not correlated (Fig. 2h).

MYC enhances PD-L1 translation through bypassing upstream open reading frame (uORF)-mediated translational repression.

We next sought to address the mechanism by which PD-L1 mRNA is inefficiently translated in $KRAS^{G12D}$ liver tumor cells, but becomes translationally activated in $MYC^{Tg};KRAS^{G12D}$. The translation of mRNAs is highly controlled by the 5′ untranslated region (5′UTR), which can contain several regulatory elements including complex structures as well as sequence-specific RNA elements[28]. To explore how PD-L1 is translationally regulated, we analyzed the 5′UtR sequence of the PD-L1 mRNA. Notably, the mouse PD-L1 mRNA contained three putative uORFs, one of which initiates from an upstream AUG (uAUG), and the other two from non-canonical upstream CUG start codons (uCUG) that partially overlaps with the main PD-L1 ORF (Fig. 3a). To molecularly validate the engagement of the ribosome on these uORFs, we performed a toeprint assay in $KRAS^{G12D}$ and $MYC^{Tg};KRAS^{G12D}$ cell lysates to directly visualize ribosome footprints on the upstream initiation codons of an in-vitro-transcribed PD-L1 5′UTR reporter. We detected that, in $KRAS^{G12D}$ cell lysate, ribosome footprints are preferably observed at the uAUG and the proximal uCUG (the uCUG near the main ORF), rather than the main AUG (Fig. 3b, RNA loading controls in Supplementary Fig. 9a). Mutating the uCUG in this reporter significantly abolished ribosome recognition of uCUG upstream start codons (Supplementary Fig. 9b). On the contrary, in $MYC^{Tg};KRAS^{G12D}$ cell lysates, the major ribosome footprints occur at the main AUG, compared to the uAUG or uCUG (Fig. 3b).

Although recent studies have identified putative uORFs genome-wide[29], little is known about the functional contribution of uORF-mediated regulation, particularly in the context of cancer development and the regulation of the immune-checkpoint molecules. To understand whether the uORFs in the 5′UtR of PD-L1 have a significant role in PD-L1 translational control, we transfected the full-length PD-L1 5′UTR upstream of a luciferase reporter in $KRAS^{G12D}$ and $MYC^{Tg};KRAS^{G12D}$ cells. We observed that the reporter activity of wild-type PD-L1 5′UTR in $MYC^{Tg};KRAS^{G12D}$ cells was significantly higher compared with that in $KRAS^{G12D}$ cells (Fig. 3c). To characterize the functionality of these uORFs, we mutated the start codons of individual uORFs (Fig. 3d). Notably, disrupting either the uCUG near the main ORF (uCUG(proximal)) or the uAUG in $KRAS^{G12D}$ cells increased the reporter activity by >100%, whereas mutating the uCUG apart from the main ORF (uCUG(distal)) had no effect (Fig. 3d). This increase in the reporter activity on proximal uCUG mutation

was less significant (~25%) in MYC^{Tg};$KRAS^{G12D}$ cells (Fig. 3e). In addition, mutating the stop codon of the uORF, which placed the proximal uCUG in frame with the main ORF, led to a significant increase in reporter activity in $KRAS^{G12D}$ cells (Supplementary Fig. 9c). We also designed a vector where the uCUG is the only initiating codon that can produce a full-length flag-tagged PD-L1 protein (uCUG-PD-Ll-FLAG). In this setting, we observed the expression of a full-length flagged-PD-Ll protein in $KRAS^{G12D}$ cells (Fig. 3f), further validating the functionality of the uCUG. Moreover, mutating both the uCUG(proximal) and the uAUG led to further enhanced reporter activity (300% increase) (Fig. 3d). These results indicate that there are two functional uORFs (uORF_1 and uORF_3 mediated by uAUG and the proximal uCUG, respectively) in mouse PD-L1 5′UTR that act in an additive manner to suppress downstream main ORF translation.

To further characterize the functional significance of these two uORFs in regulating endogenous PD-L1 translation, we used CRISPR/Cas9 genome editing to generate $KRAS^{G12D}$-derived tumor cell lines in which the proximal uCUG (Fig. 3g) or the uAUG (Supplementary Fig. 9d) in the PD-L1 mRNA 5′UTR is disrupted. Disruption of the uCUG or the uAUG start codon led to significantly enhanced protein abundance of endogenous PD-L1 compared to the non-mutated parental clone (Fig. 3g and Supplementary Fig. 9d), with no effect on PD-L1 mRNA amounts (Supplementary Fig. 9e). Dependence of these non-canonical uORFs highlights their key role in control of PD-L1 expression at the translation level. Similarly, the human PD-L1 5′UTR also contains uCUG start codon uORFs, where the initiation ribosome footprints on these uORFs can be detected in previously published ribosome-profiling datasets carried out in the presence of lactimidomycin[30], which stalls ribosomes on initiating codons (Supplementary Fig. 9f). By mutating the uCUGs in the human PD-L1 5′UTR, we observed an 100% increase in the translation of the downstream main ORF (Fig. 3h), suggesting that similar to mouse, human PD-L1 translation is also controlled by uORFs.

An outstanding question is how PD-L1 uORF-mediated translation repression is bypassed in MYC^{Tg};$KRAS^{G12D}$ cells. We observed that MYC^{Tg};$KRAS^{G12D}$ clones had significantly higher eIF2α phosphorylation amounts compared with our $KRAS^{G12D}$ clones (Fig. 3i). eIF2α is a key component of the eIF2 ternary complex[31–33] that when phosphorylated facilitates the bypass of uORFs, thereby favoring translation of the main ORF. When we treated MYC^{Tg};$KRAS^{G12D}$ cells with integrated stress response inhibitor (ISRIB), a compound selectively reverses the effects of eIF2α phosphorylation[34,35], the abundance of PD-L1 protein in MYC^{Tg};$KRAS^{G12D}$ cells was markedly downregulated (Fig. 3j), whereas PD-L1 mRNA remained unchanged (Supplementary Fig. 10). These results suggest, at least in part, a functional role for eIF2α phosphorylation in bypass of uORFs. Altogether, several orthogonal lines of evidence demonstrate that MYC elevates PD-L1 protein abundance through relieving the inhibition of PD-L1 mRNA translation mediated by functional, non-canonical uORFs.

The metastatic potential of MYC^{Tg};$KRAS^{G12D}$ tumors is dependent on PD-L1 mediated immune evasion.

Given that liver tumors that developed from MYC^{Tg};$KRAS^{G12D}$ cells expressed significantly higher PD-L1 protein abundance than $KRAS^{G12D}$ (Fig. 2c), whether the increased PD-L1 expression and subsequent immune evasion are responsible for the cancer metastatic potential remains unclear. To this end, we orthotopically injected two individual uCUG mutant $KRAS^{G12D}$ clones containing a mutation of the uORF that stimulates PD-L1 translation ($KRAS^{G12D}$ Mut clone 1 and 2), into the subcapsular region of the median liver lobe of mice (Supplementary Fig. 11a). Noteworthy, we confirmed that this immunocompetent C57BL/6 orthotopic model was able to recapitulate disease progression in a similar manner as our GEM models: C57BL/6 mice injected with tumor cells coexpressing MYC^{Tg} and $KRAS^{G12D}$ had a reduced survival time (Fig. 4a), aggressive immune infiltration in the liver (Fig. 4b and Supplementary Fig. 11b), increased PD-L1 abundance (Supplementary Fig. 11c), and increased metastatic potential (Fig. 4b,c and Supplementary Fig. 11d) when compared with those injected with $KRAS^{G12D}$ cells. In this system, $KRAS^{G12D}$ cells only developed primary tumors with no metastasis (Fig. 4c and Supplementary Fig. 11 d). Notably, 44.4 and 50% of animals injected with the two $KRAS^{G12D}$ uORF mutant clones, respectively, developed metastasis (Fig. 4c,d). These results show that increasing the translation of PD-L1 in KRAS[G12D] uORF mutant tumor cells is sufficient to facilitate metastasis, suggesting that the activity of PD-L1 on inhibiting immune surveillance is a key determinant of metastatic potential and cancer aggressiveness. Therefore, to delineate the contribution of T cell surveillance on metastases and survival, we injected MYC^{Tg};$KRAS^{G12D}$ and $KRAS^{G12D}$ cells into athymic nude mice that lack functional T cells. Ablation of T cells in nude mice ameliorated the difference in the survival rates of $KRAS^{G12D}$ and MYC^{Tg};$KRAS^{G12D}$ HCC-injected mice (Fig. 4e). Both $KRAS^{G12D}$ and MYC^{Tg};$KRAS^{G12D}$ HCC-injected athymic nude mice were able to develop pulmonary metastases (Fig. 4f), suggesting that the T cell immune surveillance normally restrains metastasis formation in $KRAS^{G12D}$-derived tumors.

eFT508, a potent clinical translation inhibitor, dramatically downregulates PD-L1 protein abundance.

Given the finding that a new layer of translational control guides PD-L1 expression, which is important for tumor development, we sought to design a rational pharmacological approach to target PD-L1 translation. Although pharmacological agents that target the core translation machinery itself may induce unwanted toxicity, targeting their post-translational modifications may offer a more favorable therapeutic window. In this respect, it is known that phosphorylation of the main cap-binding protein, eIF4E at Serine 209, positively regulates the oncogenic activity of eIF4E and promotes specific mRNA translation[36,37], whereas mutating the eIF4E phosphorylation site in knock-in mice has no effect on organismal development or physiology[36]. Similarly, ablation of the kinases responsible for phosphorylating eIF4E, mitogen-activated protein kinase interacting kinase 1 and 2 (MNK1/2), has proven to be dispensable for organismal life and the resulting mice do not show any discernible phenotypes[38]. MYC^{Tg};$KRAS^{G12D}$ cells or liver tumors do not possess higher eIF4E phosphorylation than $KRAS^{G12D}$ alone (Supplementary Fig. 12a, b), yet given the selective increase in the translational oncogenic program in MYC^{Tg};$KRAS^{G12D}$ cells,

we reasoned that these tumors may be more sensitive to inhibitors of translation. Thus, to determine whether increased PD-L1 translation can be exploited therapeutically, we used eFT508: a potent and highly selective dual MNK1/2 inhibitor[39], now in phase 2 clinical trials (NCT02937675, NCT02605083 and NCT03258398). eFT508 is considerably more potent than other reported MNK inhibitors both biochemically (MNK1 and MNK2, 2.4 and 1 nM, respectively) and in cells inhibiting phosphorylation of eIF4E (6.5 nM). Moreover, eFT508 has exceptional kinome selectivity (tested against >400 kinases) relative to reported MNK inhibitors (the nearest kinase is inhibited approximately 100-fold weaker than MNK1 or MNK2). In addition, eFT508 has excellent drug-like properties (MW 340, protein binding ~50%, $\log D = 2.7$, Caco2 A-B/B-A 15/5, excellent multi-species oral PK)[39]. In liver tumors, eFT508 efficiently eliminated eIF4E phosphorylation (Supplementary Fig. 12a) without affecting global protein synthesis (Supplementary Fig. 12c). At first, we tested the effects of eFT508 on PD-L1 expression in MYC^{Tg};$KRAS^{G12D}$ cells. Notably, inhibiting eIF4E phosphorylation by eFT508 resulted in significant and selective downregulation of MYC^{Tg};$KRAS^{G12D}$-induced PD-L1 protein abundance (Fig. 5a), but not mRNA expression (Fig. 5b); similar effects were also detected for several other translational targets upregulated in MYC^{Tg};$KRAS^{G12D}$ cells (Supplementary Fig. 12d–f). On the contrary, eFT508 had limited additional effects in reducing PD-L1 protein abundance in $KRAS^{G12D}$ cells where PD-L1 translation is suppressed (Supplementary Fig. 12g). We further found that $KRAS^{G12D}$ cells harboring mutations in the uAUG and uCUG uORFs of PD-L1 ($KRAS^{G12D}$ uAUG + uCUG_mut) exhibited reduced PD-L1 protein expression by eFT508 (Supplementary Fig. 12h), suggesting that the enhanced translation of PD-L1 can sensitize cells to this translation inhibitor. However, we cannot at present exclude a potentially more direct effect of eIF4E phosphorylation on uORF-mediated translational repression. Moreover, the effects of eFT508 on PD-L1 translation can be mirrored genetically in eIF4E phosphorylation-ablated ($Eif4e^{S209A/S209A}$) mice[36] that show a 50% decrease in PD-L1 protein expression compared with wild type when livers of these animals are transfected with MYC and $KRAS^{G12D}$ in vivo (Fig. 5c and Supplementary Fig. 12i).

eFT508 prevents liver cancer progression and metastasis in vivo.

Given that there was a marked inhibitory effect on PD-L1 by eFT508 treatment in MYC^{Tg};$KRAS^{G12D}$ HCC cells, but not in $KRAS^{G12D}$ cells, we next examined whether eFT508 could prevent tumor progression in the MYC^{Tg};$KRAS^{G12D}$ orthotopic preclinical model. Daily oral treatment of eFT508 reduced primary tumor growth (Supplementary Fig. 12j), doubled the survival time of C57BL/6 mice bearing MYC^{Tg};$KRAS^{G12D}$ tumors (Fig. 5d), and prevented lung metastasis formation (Fig. 5e). Moreover, eFT508 led to a marked inhibition of eIF4E phosphorylation and 50% reduction in PD-L1 abundance in vivo (Fig. 5f), which recapitulated our in vitro findings. Of note, eFT508 had no effect in mice bearing $KRAS^{G12D}$ tumors (Fig. 5g), suggesting that although more aggressive, MYC^{Tg};$KRAS^{G12D}$ tumors are more sensitive to eFT508 treatment, as they rely on PD-L1 translation for their progression. The possibility of the presence of an HA model antigen derived from the HA-tag linked to MYC transgene does not influence the immune microenvironment (Supplementary Fig. 13a,b) nor the sensitivity to eFT508 treatment (Supplementary Fig. 13c).

To further address whether inhibiting the PD-1/ PD-L1 functional complex could mimic the anti-tumor effect of eFT508, we treated the MYC^{Tg};$KRAS^{G12D}$ orthotopic model with monoclonal antibodies against PD-1. Treatment with anti-PD-1 resulted in a significant increase in survival (Fig. 5h), suggesting that targeting the PD-1/PD-L1 axis can markedly reduce the aggressiveness of MYC^{Tg};$KRAS^{G12D}$ tumors. However, unlike the monoclonal antibodies against PD-L1 that also target and may kill immune cells in the tumor microenvironment that express PD-L1[40,41], eFT508 has a high selectivity against the PD-L1 protein on tumor cells, but not the infiltrated myeloid cells, liver-resident macrophages, and T cells (where PD-L1 expression is relatively low in our tumor model) (Supplementary Fig. 14a,b). Furthermore, eFT508 treatment resulted in a significant increase in cytotoxic CD8+ T cells compared with untreated tumors (Fig. 5i) that were positive in cytotoxic anti-tumor activity as assessed by surface CD107A abundance[42] (Fig. 5j). Together, these findings reveal a key molecular underpinning of the immune response in acquiring metastatic potential, the leading cause of cancer lethality, and highlight that oncogene-mediated translational control of the immune checkpoint is effectively targeted with eFT508 specifically in tumor cells without affecting immune cells, maximizing the anti-tumor effect.

Discussion

Oncogenes widely manipulate many diverse gene expression programs to direct cancer progression. Given the fact that we have profiled two end-stage tumor types ($KRAS^{G12D}$ and MYC^{Tg};$KRAS^{G12D}$ tumors), during the course of their evolution, similar transcriptome profiles may have been co-opted and are consistent with Myc hyperactivation in fully developed Ras tumors. Instead, a more profound remodeling of gene expression at the step of translation control offers unique gene regulatory programs to selectively synthesize effector proteins in unique stages of cancer development, for example, to shape the tumor microenvironment (Fig. 2b). The broader implication of our data is that translational regulation of the immune regulators facilitates tumor cells evasion from immune attack to promote tumor progression and metastasis, and this regulation is not typically detected by standard methodologies that profile cancer cells (that is, genomics and transcriptomics). In particular, although a potent uORF embedded in the PD-L1 5′ UTR serves as the main obstacle for the efficient translation of PD-L1 mRNA, this mechanism leaves a 'backdoor' for specific oncogenes, such as MYC, to re-activate PD-L1 translation at least in part by hijacking the phospho-eIF2α dependent adaptive stress pathway, which has been previously linked to the oncogenic activity of MYC[43]. Cancer cells may use this unique mechanism to more rapidly synthesize PD-L1 protein (compared with transcriptional control), in response to tumor immune environment changes, allowing for tumor progression and metastasis. It is also important to note that genetic alterations in regulatory elements in the 3′ untranslated region of PD-L1 increase PD-L1 expression[44] and it will be interesting to determine the interplay between translation control and mRNA stability of this key checkpoint protein. In this respect, a selective, clinically relevant translational inhibitor, eFT508, exhibits remarkable sensitivity when the translation of the immune-check-point protein is hyperactive. In addition, while this manuscript was in press, a recent study has shown that components of the translation initiation complex, eIF4F, can also affect PD-L1 expression through the translational upregulation of STAT1, a transcription factor controlling PD-L1

expression[45]. Together with our work, this suggests that key immune-checkpoint proteins can be regulated by translation factors at many levels and that translation inhibitors may serve as important drugs for immunotherapies. In the context of liver cancer, our findings are significant as HCC is a major cause of cancer death worldwide with surgical resection as the only means to manage the disease, yet most patients are not suitable for surgery because of poor hepatic reserve and metastatic lesions. Furthermore, as the amplification and activation of MYC and RAS are among the most frequent lesions that cooperate in many human cancers[19,46,47], translational control of the immune checkpoint is likely to be more widespread in many cancer types.

It remains poorly understood why only a fraction of cancer patients respond to immune-checkpoint antibody blockade, and resistance to immune-checkpoint inhibitors has been reported in cancer patients[48]. With respect to our ribosome-profiling data, besides PD-L1, there are several other key factors or pathways involved in cell cycle regulation, tumor cell motility and immune response that are upregulated by Ribo-Seq in tumors with MYC hyperactivation (Supplementary Figs. 5 and 6), which are also effectively targeted by the translation inhibitor eFT508 (Supplementary Fig. 12). Therefore, selective inhibitors of mRNA translation, such as eFT508, may have the potential to both enhance anti-tumor immune response and inhibit cancer progression and metastasis, offering a therapeutic approach that could improve therapeutic efficacy over existing checkpoint inhibitors and could be further combined to achieve beneficial outcomes.

Online content

Any methods, additional references, Nature Research reporting summaries, source data, statements of data availability and associated accession codes are available at https://doi.org/10.1038/s41591–018-0321–2.

Methods

Mice.

A modified pCAGEN vector[49] containing PmeI sites flanking the CAG promoter[50] and rabbit beta-1 globin gene polyadenylation sites was used to as the backbone of the transgenic vector. Cloning of a Lox-STOP-Lox element[51], N-terminal HA-epitope tagged *c-MYC* (human), encephalomyocarditis virus internal ribosome entry site[52], and palmitoylated-eGFP[53] was performed to insert these sequences in the multi cloning site located between the CAG promoter and the downstream beta-1 globin gene untranslated sequences containing polyadenylation sites to generate a Cre-activateable bicistronic mRNA capable of simultaneous expression of HA-tagged MYC and palmitoylated GFP in a wide array of cells and tissues. MYC^{Tg} mice were created via pronuclear injection of the purified PmeI digested fragment containing the transgene sequence into C57Bl/6 zygotes by the Gladstone Institutes transgenic core facility. Our MYC^{Tg} mice has a similar MYC overexpression range to human HCC. The LSL-$KRAS^{G12D}$ mouse (a point mutation endogenous $KRAS$ locus) was purchased from The Jackson Laboratory, and mice with liver-specific $KRAS^{G12D}$ expression ($Alb\ Cre;\ KRAS^{G12D}$) were generated. To generate $Alb\ Cre;MYC^{Tg};KRAS^{G12D}$ mice, we intercrossed the MYC^{Tg} mouse to the $Alb\ Cre;\ KRAS^{G12D}$ mouse. The University

of California San Francisco Institutional Animal Care and Use Committee approved all studies involving live mice.

In vivo sample preparation.

Mouse liver tumors were micro-dissected immediately after animal euthanization. Liver perfusion (with ice-cold PBS containing 10 mg ml^{-1} cycloheximide). Wild-type liver or the micro-dissected tumors were snap frozen in liquid nitrogen, followed by grounding with mortar and pestle. Tumor was resuspended in the lysis buffer (20 mM Tris pH 7.5, 150 mM NaCl, 15 mM MgCl$_2$, 100 μg ml^{-1} cycloheximide, 1 mM DTT, 0.5% Triton X-100, 0.1 mg ml^{-1} heparin, 8% glycerol, 20 U per ml TURBO DNase, ×1 Combined Protease and Phosphatase Inhibitor).

Deep-sequencing library preparation.

The ribosome-profiling analysis was carried out as described previously[54]. Briefly, after removing the nuclei and mitochondria, lysate was treated with RNase A/T1 mix (0.5 mg RNase A (Ambion, AM2272) and 1,000 U RNase T1 (Life Technologies, 2280)) to digest mRNAs that are not protected by the ribosome. The digestion was stopped by adding SUPERase-In RNase Inhibitor (20 U per μl, Ambion, AM2696), followed by centrifuging to pellet ribosomes. Ribosome-protected fragments were purified by TRIzol, and two biological replicates were performed for each type of Ribo-Seq and all Ribo-Seq libraries (three biological replicates for wild-type liver).

Analysis of RNA-Seq and Ribo-Seq libraries.

A layered alignment was performed to first discard reads mapping to mouse ribosomal RNA (rRNA) sequences using Burrows–Wheeler Aligner[55]. Non-rRNA reads were then aligned against the mouse transcriptome (GRCm38 build 76) using RSEM[56] and bowtie2 [57]. Reads were aligned strand-specifically to exclude anti-sense or other non-transcript reads. For each gene, total number of ribosome-protected fragments and RNA reads were counted and fed into the downstream analysis. A minimum of two counts per million in at least two Ribo-Seq libraries was used as a cutoff to filter out lowly expressed genes, following the guideline[58]. Differential gene expression analyses were performed using the limma package[59] with voom method[60]. Briefly, the effective library size of each deep-sequencing library was calculated and raw read count data were normalized by the trimmed mean of M values method[61]. Normalized read counts were reported in Supplementary Tables 1 and 2. Variance-mean relationship in count data was estimated using the voom method[60] and differential gene expression was tested using a model of negative binomial distribution. A linear regression was performed to the normalized read counts, as a function of sample type variables ('WT', '$KRAS^{G12D}$' or 'MYC^{Tg};$KRAS^{G12D}$'). Here, the coefficient of sample type variables (that is, 'MYC^{Tg};$KRAS^{G12D}$' over '$KRAS^{G12D}$') is a measurement of corresponding differential gene expressions. P values were adjusted using the Benjamini–Hochberg procedure for multi-testing, and these adjusted P values (P_{adj} or false discovery rate) were reported for each gene in Supplementary Data. To visualize the deep-sequencing datasets, sequencing reads were aligned to the mouse genome (GRCm38) using the STAR RNA-Seq aligner[62], and imported into the Integrative Genomics Viewer[63].

For the comparison of the similarity of human liver cancer and mouse liver cancer: human liver hepatocellular carcinoma and normal liver samples were based on data generated by The Cancer Genome Atlas Research Network (http://cancergenome.nih.gov/). Raw estimated number of reads that aligned to each transcript were obtained for 370 primary tumors and 50 normal liver samples from FireBrowse (http://firebrowse.org/). Differential gene expression analyses were performed similar as for the mouse samples. Here, a linear regression was performed to the normalized read counts, as a function of sample type variables ('primary tumor' or 'normal'). The coefficient of sample type variables ('primary tumor' over 'normal') is a measurement of differential gene expressions. P values were adjusted using the Benjamini–Hochberg procedure for multi-testing.

Gene functional analyses and visualization.

Gene Ontology enrichment and clustering analysis was carried out using ClueGO[64] for genes that are upregulated in Ribo-Seq comparing $MYC^{Tg};KRAS^{G12D}$ to $KRAS^{G12D}$ ($P_{adj} < 0.1$ and $\log_2 FC > 2$). The following parameters were used: Reference set: all genes analyzed; Enrichment: right-sided hypergeometric test, P value adjustment: Benjamini–Hochberg adjustment. Enriched gene ontology terms were then grouped using Kappa statistics with leading group term on the basis of the highest statistical significance. Protein interaction networks were retrieved from STRING v.10.0 database[65] and imported into Cytoscape[66] for visualization. Each node represents a gene and edges show protein-protein association with width proportional to the association score. Disconnected nodes were removed from the plot for simplicity.

Plasmids.

PD-L1 5′UTR was synthesized and cloned into the HindIII and NcoI sites of pGL3-SV40 control vector (Promega). CUG and STOP mutations were carried out using site-direct mutagenesis. PD-L1 5′UTR, CDS and 3′UTR fused with a FLAG sequence were amplified and cloned into murine stem cell virus backbone vector. CDS start codon ATG deletion and frame shift ('TG' removal from 'ATG') were generated by site-direct mutagenesis. Human MYC, a T2A peptide sequence and $KRAS^{G12D}$ were together cloned into a murine stem cell virus backbone vector. Sequences were based off the NCBI database.

Immunofluorescence.

Liver and lung tissues were dissected from mice and fixed in 10% formalin overnight at 4 °C. Tissues were subsequently dehydrated in ethanol at room temperature, mounted into paraffin blocks and sectioned at 5 μm. Specimens were de-paraffinized, rehydrated, and antigen unmasking was performed as previously described[54]. The sections were then incubated in 5% goat serum, 1% BSA in tris-buffered saline for 1 h at room temperature. Primary antibodies were diluted 1:50–1:500 in blocking solution and incubated on sections overnight at 4 °C. Specimens were incubated with the appropriate Alexa 488 and 594 labeled secondary (Invitrogen) at 1:500 for 2 h at room temperature after washing, followed by mounting with DAPI Hardset Mounting Medium (Vector Lab). Zeiss AxioImager M1 microscope was used to image. Individual cells were quantified for mean fluorescence intensity using the Axiovision (Zeiss, Release 4.8) densitometric tool.

H&E staining.

Paraffin-embedded liver and lung specimens were de-paraffinized and rehydrated, and stained with hematoxylin (Thermo Scientific), followed with washes with water. An incubation in differentiation RTU (VWR) and two washes with water followed by two 70% ethanol washes were performed. The samples were then stained with eosin (Thermo Scientific) then dehydrated with ethanol followed by CitriSolv (Fisher). Slides were mounted with Cytoseal XYL (Richard Allan Scientific).

Luciferase assay.

$KRAS^{G12D}$ and MYC^{Tg};$KRAS^{G12D}$ cells were transfected in 12-well plates with 200 ng of pGL3 (Firelfy luciferase) constructs containing full-length or mutant 5′UTR of PD-L1 and 40 ng of pRL (Renilla luciferase) plasmid using Lipofectamine 2000 (Invitrogen) according to the manufacturer's instructions. Cells were collected 24 h post-transfection and half of the cells were assayed using Dual luciferase kit (Promega), the other half were proceeded for TRIzol (Invitrogen) purification of RNA. Firefly luciferase activity was normalized to Renilla activity, and further normalized to Firefly and Renilla luciferase RNA amounts quantified by RT-qPCR.

Western blotting.

Western blots were performed with antibodies against of GFP (Abcam no. ab290, 1:2,000), MYC (Cell Signaling no. 5605, 1:1,000), β-actin (Sigma no. A5316, 1:10,000), ARG1 (Sigma no. HPA024006, 0.4 µg ml^{-1} for western blot), RAS^{G12D} (Cell Signaling no. 14429, 1:1,000), p-eIF2α Ser51 (Cell Signaling no. 3597, 1:500), eIF2α (Cell Signaling no. 9722, 1:1,000), p-eIF4E Ser209 (Cell Signaling no. 9721, 1:1,000), eIF4E (BD no. 610270, 1:1,000), GAPDH (Cell Signaling no. 2118, 1:1,000), p-ERK1/2 (Cell Signaling no. 4370, 1:1,000), SNAIL (Proteintech, 13099–1-AP, 1:500), CDC20 (Proteintech, 10252–1-AP, 1:1,000), PLK1 (Proteintech, 10305–1-AP, 1:1,000), ADAM8 (Proteintech, 23778–1-AP, 1:1,000), RPS2 (Abcam, ab58341, 1:1,000), HA-HRP (Cell Signaling no. 2999, 1:1,000), HSP90 (Cell Signaling, no. 4877, 1:1,000), and PD-L1 (Cell Signaling, no. 13684, 1:1,000). Blots are developed using ChemiDoc Imaging Systems (BioRad).

Sucrose gradient fractionation.

$KRAS^{G12D}$ and MYC^{Tg};$KRAS^{G12D}$ cells were treated with 0.1 mg ml^{-1} Cycloheximide for 5 min, before lysing in 300 µl of lysis buffer (20 mM Tris pH 7.5, 200 mM NaCl, 15 mM MgCl$_2$, 1 mM DTT, 1% Triton X-100, 0.1 mg ml^{-1} cycloheximide, 200 U per ml RNasin (Promega)). Nuclei and membrane debris was then removed by centrifuging at 10,000g, for 5 min. The lysate was loaded onto a sucrose gradient (10–50% sucrose(w/v), 20 mM Tris pH 7.5, 100 mM NaCl, 15 mM MgCl$_2$ and centrifuged in a SW41Ti rotor (Beckman) for 2.5 h at 38,000 r.p.m. at 4 °C. Fractions were collected by density gradient fractionation system (Teledyne ISCO).

qPCR.

RNA was isolated using TRIzol (Invitrogen) purification using PureLink RNA Mini Kit (Thermo Fisher, 12183018). RNAs were converted into cDNAs using High-Capacity cDNA

Reverse Transcription Kit (Thermo Fisher Scientific). cDNAs were diluted 1 to 10, and used for SYBR green detection RT-qPCR assay. Primers were used at 250 nM per reaction. *Cd274* F 5′-AGTCTCCTCGCCTG CAGATA, *Cd274* R 5′-AGTAAACGCCCGTAGCAAGT. *Gapdh* F 5′- C A ATG A ATACGGCTACAGCAA, *Gapdh* R 5′-AGGGAGATGCTCAGTGTTGG. *Fluc* F 5′ -CAACTGCATAAG GCTATGAAGAGA, *Fluc* R 5′-ATTTGTATTCAGCCCATATCGTTT. *Rluc* F 5′-CAAAGAG AAAGGTGAAGTTCGTC, *Rluc* R 5′- TGTACAACGTCAGGTTTACCAC.

Hydrodynamic tail vein injection.

Plasmid DNA was injected by hydrodynamic technique as previously described[67]. Briefly, endotoxin-free plasmid DNA was prepared using Qiagen Endo Free Maxi Kit and dissolved in Saline solution to a final volume of 8% of body weight at room temperature. 8–10-week-old gender-matched mice were used for comparison. They were restrained and the lateral tail vein was accessed with a 26 G needle. Each mouse was administrated with 10 μg of dissolved DNA and the administration of the solution was performed in 10 s or less without extravasation.

Flow cytometry.

Cultured cell lines were detached and gathered with ×1 citric saline. Primary hepatocytes were collected from mice and prepared with liver dissociation kit (Miltenyi Biotech, 130–105-807) according to the manufacturer instructions. Mouse anti-PD-L1 antibody (BioLegend, 124314) were then added to single cell suspension, followed by incubation for 30 min at 4 °C. Data were acquired through a BD FACSVerse and were analyzed with FlowJo software (Tree Star).

Immune profiling.

Mice were euthanized at described post-natal ages and when clinically indicated due to terminal burden of disease. After euthanasia, the thoracic cavity was revealed and 24 G butterfly needle was inserted into the left ventricle. Distal tissues were perfused using instillation of 20 ml of PBS until blanching of the liver is observed. Harvested livers were minced with sterile scalpels before transfer into GentleMACS C Tubes (Miltenyi Biotec). Digestion media with enzyme composition per Miltenyi Liver Dissociation Kit (5 ml) was added to each tube and digestion to single cell suspension performed using GentleMACS on program '37_m_LIDK_1'. Digestion was then filtered through 70 μm mesh and washed with 20 ml PBS followed by centrifugation at 450g for 8 min at 4 °C. Red blood cells were lysed by resuspension of the pellet in 5 ml of ACK lysis buffer (ThermoFisher). Lysis quenched after 3 min with 25 ml of ice cold FACS (PBS with 0.5% BSA and 5 mM EDTA) buffer. Suspension again pelleted by centrifugation at 450 g for 8 min at 4 °C. Resulting pellet was resuspended in 5 ml of RPMI-L (RPMI supplemented with 5% FBS and 5 mM EDTA) and overlayed onto 10 ml of Lymphoprep (StemCell Technologies) followed by centrifugation at 800 g for 25 min at room temperature. Isolated aqueous- and interphases were collected and washed with FACS buffer by spinning down at 300g for 5 min at 4 °C. Mononuclear cells were counted and aliquoted to 1×10^7 cells before staining for flow cytometry.

For analysis of infiltrating mononuclear cells, isolated cells were blocked with CD16/32 FcB (Cell Culture Facility, UCSF) for 15 min on ice. Samples were then divided into two fractions for staining of either Lymphoid or Myeloid cell markers for 45 min on ice in dark. Lymphoid markers were analyzed by staining APC-CD45, PECy7-CD3, PB-CD19, PE-CD4, and PerCPCy5.5-CD8. Myeloid markers were analyzed by staining APC-CD45, PECy7-Ly6G/C, PE-CD11c, PerCPCy5.5-CD14, and Bv510-CD11b. All antibodies were purchased from eBioscience. Samples were then acquired by BD LSR II (Becton Dickinson) and analyzed with FlowJo (FlowJo, LLC).

Generating mice liver cancer cell lines.

Alb-Cre; KRAS^{G12D} and *Alb-Cre; MYC*^{Tg};*KRAS*^{G12D} mice were anesthetized and disinfected with 70% ethanol. Abdomen and chest were exposed and then portal vein was cut, followed immediately by cannulating the thoracic SVC via atrium to clear the blood using a breathing apparatus. The surface of the liver was wet with L-15 solution. The liver was then rinsed with the Liver Perfusion Media (GIBCO cat. no. 17701–038) for 4 min, followed by perfusion with the liver digest media (GIBCO cat. no. 17703–034) for 4–8 min. After a sufficient digestion, the liver was isolated and transferred to a sterile plastic petri dish in a cell culture hood. The liver was then minced in the hepatocyte plating medium (DMEM H21 high glucose medium supplied with ×1 Pen/Strep solution, ×1 insulin-transferrin-selenium solution (GIBCO no. 41400–045) and 5% FBS) and filtered through a sterile gauze into a 50 ml conical tube. Cells were washed with and resuspended in hepatocyte plating medium and plated on a sterile plastic petri dish for culturing. Cells were then plated into 96-well plates for single cell selection. *KRAS*^{G12D} and *MYC*^{Tg};*KRAS*^{G12D} single clonal cancer cells were confirmed by western blot and immunofluorescence with MYC, *KRAS*^{G12D}, ARG1 and HA antibodies.

Toeprint assay.

Mouse PD-L1 5′UTR sequence was cloned into pGL3 (Firefly luciferase) vector that contains a T7 promoter. mRNA was in vitro transcribed using mMESSAGE mMACHINE T7 Transcription Kit (Thermo Fisher Scientific). The reverse transcription oligonucleotide (TATCTCTTCATAGCCTTATG) was [γ–^{32}P]ATP labeled, and pre-annealed to the mRNA by heating for 1 min at 65 °C followed by 37 °C for 8 min in 40 mM Tris-HCl (pH 7.5) and 0.2 mM EDTA. Cytoplasmic cell lysates from *KRAS*^{G12D} and *MYC*^{Tg};*KRAS*^{G12D} cells were extract and incubated with the oligo-mRNA complex, followed by reverse transcription as previously described[68]. cDNA products were extracted with phenol and analyzed on 8% TBE gels.

CRISPR in the *Alb-Cre; KRAS*^{G12D} cell line.

A guide RNA (sgRNA) against *Cd274* uORF sequence was designed from the F. Zhang laboratory database (crispr.mit.edu)[69], and cloned into pSpCas9(BB)-2A-GFP (PX458) vector (Addgene no. 48138)[69]. Non-targeting control sgRNA was used side-by-side with *Cd274* sgRNA to rule out phenotypes result from nonspecific editing. To obtain single clonal cell lines, GFP-positive cells were sorted into 96-well plates. Genomic DNAs were isolated, PCR amplified and sequenced to confirm editing. PD-L1 protein changes were detected by

flow cytometry. *Cd274* sgRNA (targeting uCUG): 5′-GGGCCAGTCTCCTCGCCTGC-3′. *Cd274* sgRNA (targeting uAUG): 5′-TGGTCCCCAAGCCTCATGCC-3′.

Intrahepatic metastatic HCC graft implantation and drug treatment.

Ex vivo cultures of primary, single-clone cell lines from individual liver tumors were derived from one *Alb-Cre; KRAS^{G12D}* and one *Alb-Cre; MYC^{Ts}*;*KRAS^{G12D}* mice. HCC cells described above were trypsinized, counted and 5×10^5 of cells were injected into the subcapsular region of the median liver lobe of C57BL/6 mice. Analgesics including bupivacaine and buprenorphine were given to the mice, while meloxicam was not given as it may have an effect on the tumor immune microenvironment. Primary liver tumor formation was detected at day 4. Over 70% of the mice successfully develop lung metastasis at days 12–18. Mice were treated daily 7 d post-injection of tumor cells with 10 mg kg^{-1} of eFT508 or vehicle control through oral gavage.

Statistics.

Data were represented as mean ± s.d. Sample sizes were chosen on the basis of previous literature, or decided by using a power analysis (power/sample size calculator) on the basis of pilot experiments that provided an estimate of effect size. For in vivo experiments in mice, an $n = 4$ was the minimum amount used. Data were analyzed and statistics performed in Microsoft Excel and/or GraphPad Prism6. A two-tailed, unpaired Student's *t* test was used for pair-wise comparison. For correlation analysis, a two-sided Pearson's correlation test was used. For survival analysis, a log-rank test or Wilcoxon rank sum test was used. $P < 0.05$ was considered significant, and the exact *P* values are indicated in the figures.

Ethical compliance.

All experiments involving live vertebrates performed at UCSF were done in compliance with ethical regulations approved by the UCSF IACUC committee. Protocols for human sample collection and analysis were approved by UCSF, and all analyses of human data were carried out in compliance with the relevant ethical regulations.

Supplementary Material

Refer to Web version on PubMed Central for supplementary material.

Acknowledgements

References

1. Chen DS & Mellman I Oncology meets immunology: the cancer-immunity cycle. Immunity 39, 1–10 (2013). [PubMed: 23890059]

2. Casey SC et al. MYC regulates the antitumor immune response through CD47 and PD-L1. Science 352, 227–231 (2016). [PubMed: 26966191]

3. Marzec M et al. Oncogenic kinase NPM/ALK induces through STAT3 expression of immunosuppressive protein CD274 (PD-L1, B7-H1). Proc. Natl Acad. Sci. USA 105, 20852–20857 (2008). [PubMed: 19088198]

4. Stewart BW & Wild C World Cancer Report 2014 (International Agency for Research on Cancer WHO Press, 2014).

5. Ally A et al. Comprehensive and integrative genomic characterization of hepatocellular carcinoma. Cell 169, 1327 (2017). [PubMed: 28622513]

6. Schlaeger C et al. Etiology-dependent molecular mechanisms in human hepatocarcinogenesis. Hepatology 47, 511–520 (2008). [PubMed: 18161050]

7. Marquardt JU et al. Sequential transcriptome analysis of human liver cancer indicates late stage acquisition of malignant traits. J. Hepatol. 60, 346–353 (2014). [PubMed: 24512821]

8. Kaposi-Novak P et al. Central role of c-Myc during malignant conversion in human hepatocarcinogenesis. Cancer Res. 69, 2775–2782 (2009). [PubMed: 19276364]

9. O'Dell MR et al. Kras(G12D) and p53 mutation cause primary intrahepatic cholangiocarcinoma. Cancer Res. 72, 1557–1567 (2012). [PubMed: 22266220]

10. Saha SK et al. Mutant IDH inhibits HNF-4alpha to block hepatocyte differentiation and promote biliary cancer. Nature 513, 110–114 (2014). [PubMed: 25043045]

11. Grivennikov SI, Greten FR & Karin M Immunity, inflammation, and cancer. Cell 140, 883–899 (2010). [PubMed: 20303878]

12. Sato E et al. Intraepithelial CD8+tumor-infiltrating lymphocytes and a high CD8+/regulatory T cell ratio are associated with favorable prognosis in ovarian cancer. Proc. Natl Acad. Sci. USA 102, 18538–18543 (2005). [PubMed: 16344461]

13. Gao Q et al. Intratumoral balance of regulatory and cytotoxic T cells is associated with prognosis of hepatocellular carcinoma after resection. J. Clin. Oncol. 25, 2586–2593 (2007). [PubMed: 17577038]

14. Fu JL et al. Increased regulatory T cells correlate with CD8 T-cell impairment and poor survival in hepatocellular carcinoma patients. Gastroenterology 132, 2328–2339 (2007). [PubMed: 17570208]

15. Fridman WH, Pages F, Sautes-Fridman C & Galon J The immune contexture in human tumours: impact on clinical outcome. Nat. Rev. Cancer 12, 298–306 (2012). [PubMed: 22419253]

16. Tumeh PC et al. PD-1 blockade induces responses by inhibiting adaptive immune resistance. Nature 515, 568–571 (2014). [PubMed: 25428505]

17. Mellman I, Coukos G & Dranoff G Cancer immunotherapy comes of age. Nature 480, 480–489 (2011). [PubMed: 22193102]

18. Joyce JA & Fearon DT T cell exclusion, immune privilege, and the tumor microenvironment. Science 348, 74–80 (2015). [PubMed: 25838376]

19. Kortlever RM et al. Myc cooperates with Ras by programming inflammation and immune suppression. Cell 171, 1301–1315 e1314 (2017). [PubMed: 29195074]

20. Ingolia NT, Ghaemmaghami S, Newman JRS & Weissman JS Genome-wide analysis in vivo of translation with nucleotide resolution using ribosome profiling. Science 324, 218–223 (2009). [PubMed: 19213877]

21. Butte MJ, Keir ME, Phamduy TB, Sharpe AH & Freeman GJ Programmed death-1 ligand 1 interacts specifically with the B7–1 costimulatory molecule to inhibit T cell responses. Immunity 27, 111–122 (2007). [PubMed: 17629517]

22. Herbst RS et al. Predictive correlates of response to the anti-PD-L1 antibody MPDL3280A in cancer patients. Nature 515, 563–567 (2014). [PubMed: 25428504]

23. Gordon SR et al. PD-1 expression by tumour-associated macrophages inhibits phagocytosis and tumour immunity. Nature 545, 495–499 (2017). [PubMed: 28514441]

24. Shalapour S et al. Immunosuppressive plasma cells impede T-cell-dependent immunogenic chemotherapy. Nature 521, 94–U235 (2015). [PubMed: 25924065]

25. Khan AR et al. PD-L1hi B cells are critical regulators of humoral immunity. Nat. Commun. 6, 5997 (2015). [PubMed: 25609381]

26. Lau J et al. Tumour and host cell PD-L1 is required to mediate suppression of anti-tumour immunity in mice. Nat. Commun. 8, 14572 (2017). [PubMed: 28220772]

27. Gollwitzer ES et al. Lung microbiota promotes tolerance to allergens in neonates via PD-L1. Nat. Med. 20, 642–647 (2014). [PubMed: 24813249]

28. Truitt ML & Ruggero D New frontiers in translational control of the cancer genome. Nat. Rev. Cancer 17, 332 (2017).

29. Sendoel A et al. Translation from unconventional 5′ start sites drives tumour initiation. Nature 541, 494–499 (2017). [PubMed: 28077873]

30. Stern-Ginossar N et al. Decoding human cytomegalovirus. Science 338, 1088–1093 (2012). [PubMed: 23180859]

31. Calkhoven CF, Muller C & Leutz A Translational control of C/EBP alpha and C/EBP beta isoform expression. Gene Dev. 14, 1920–1932 (2000). [PubMed: 10921906]

32. Palam LR, Baird TD & Wek RC Phosphorylation of eIF2 facilitates ribosomal bypass of an inhibitory upstream ORF to enhance CHOP translation. J. Biol. Chem. 286, 10939–10949 (2011). [PubMed: 21285359]

33. Starck SR et al. Translation from the 5′ untranslated region shapes the integrated stress response.Science 351, 3867 (2016).

34. Sekine Y et al. Stress responses. Mutations in a translation initiation factor identify the target of a memory-enhancing compound. Science 348, 1027–1030 (2015). [PubMed: 25858979]

35. Sidrauski C, McGeachy AM & Ingolia NT & Walter P The small molecule ISRIB reverses the effects of eIF2alpha phosphorylation on translation and stress granule assembly. Elife 4, 05033 (2015).

36. Furic L et al. eIF4E phosphorylation promotes tumorigenesis and is associated with prostate cancer progression. Proc. Natl Acad. Sci. USA 107, 14134–14139 (2010). [PubMed: 20679199]

37. Herdy B et al. Translational control of the activation of transcription factor NF-kappaB and production of type I interferon by phosphorylation of the translation factor eIF4E. Nat. Immunol. 13, 543–550 (2012). [PubMed: 22544393]

38. Ueda T, Watanabe-Fukunaga R, Fukuyama H, Nagata S & Fukunaga R Mnk2 and Mnk1 are essential for constitutive and inducible phosphorylation of eukaryotic initiation factor 4E but not for cell growth or development. Mol. Cell. Biol. 24, 6539–6549 (2004). [PubMed: 15254222]

39. Reich SH et al. Structure-based design of pyridone-aminal eFT508 targeting dysregulated translation by selective mitogen-activated protein kinase interacting kinases 1 and 2 (MNK1/2) inhibition. J. Med. Chem. 26, 3516–3540 (2018).

40. Pulko V et al. B7-H1 expressed by activated CD8 T cells is essential for their survival. J. Immunol. 187, 5606–5614 (2011). [PubMed: 22025548]

41. Liu X et al. B7-H1 antibodies lose antitumor activity due to activation of p38 MAPK that leads to apoptosis of tumor-reactive CD8(+) T cells. Sci. Rep. 6, 36722 (2016). [PubMed: 27824138]

42. Betts MR et al. Sensitive and viable identification of antigen-specific CD8+ T cells by a flow cytometric assay for degranulation. J. Immunol. Methods 281, 65–78 (2003). [PubMed: 14580882]

43. Hart LS et al. ER stress-mediated autophagy promotes Myc-dependent transformation and tumor growth. J. Clin. Invest. 122, 4621–4634 (2012). [PubMed: 23143306]

44. Kataoka K et al. Aberrant PD-L1 expression through 3′-UTR disruption in multiple cancers. Nature 534, 402 (2016). [PubMed: 27281199]

45. Cerezo M et al. Translational control of tumor immune escape via the eIF4F-STAT1-PD-L1 axis in melanoma. Nat. Med. 24, 1877–1886 (2018). [PubMed: 30374200]

46. D'Cruz CM et al. c-MYC induces mammary tumorigenesis by means of a preferred pathway involving spontaneous Kras2 mutations. Nat. Med. 7, 235–239 (2001). [PubMed: 11175856]

47. Ying HQ et al. Oncogenic kras maintains pancreatic tumors through regulation of anabolic glucose metabolism. Cell 149, 656–670 (2012). [PubMed: 22541435]

48. Sharma P, Hu-Lieskovan S, Wargo JA & Ribas A Primary, adaptive, and acquired resistance to cancer immunotherapy. Cell 168, 707–723 (2017). [PubMed: 28187290]

49. Matsuda T & Cepko CL Electroporation and RNA interference in the rodent retina in vivo and in vitro. Proc. Natl Acad. Sci. USA 101, 16–22 (2004). [PubMed: 14603031]

50. Miyazaki J et al. Expression vector system based on the chicken beta-actin promoter directs efficient production of interleukin-5. Gene 79, 269–277 (1989). [PubMed: 2551778]

51. Jackson EL et al. Analysis of lung tumor initiation and progression using conditional expression of oncogenic K-ras. Gene Dev. 15, 3243–3248 (2001). [PubMed: 11751630]

52. Rees S et al. Bicistronic vector for the creation of stable mammalian cell lines that predisposes all antibiotic-resistant cells to express recombinant protein. Biotechniques 20, 102–104,106, 108–110 (1996).

53. Okada A, Lansford R, Weimann JM, Fraser SE & McConnell SE Imaging cells in the developing nervous system with retrovirus expressing modified green fluorescent protein. Exp. Neurol. 156, 394–406 (1999). [PubMed: 10328944]

54. Hsieh AC et al. The translational landscape of mTOR signalling steers cancer initiation and metastasis. Nature 485, 55–61 (2012). [PubMed: 22367541]

55. Li H & Durbin R Fast and accurate short read alignment with Burrows–Wheeler transform. Bioinformatics 25, 1754–1760 (2009). [PubMed: 19451168]

56. Li B & Dewey CN RSEM: accurate transcript quantification from RNA-Seq data with or without a reference genome. BMC Bioinformatics 12, 323 (2011). [PubMed: 21816040]

57. Langmead B & Salzberg SL Fast gapped-read alignment with Bowtie 2. Nat. Methods 9, 357–U354 (2012). [PubMed: 22388286]

58. Chen Y, Lun AT & Smyth GK From reads to genes to pathways: differential expression analysis of RNA-Seq experiments using Rsubread and the edgeR quasi-likelihood pipeline. FI000Res. 5, 1438 (2016).

59. Ritchie ME et al. limma powers differential expression analyses for RNA-sequencing and microarray studies. Nucleic Acids Res. 43, e47 (2015). [PubMed: 25605792]

60. Law CW, Chen YS, Shi W & Smyth GK voom: precision weights unlock linear model analysis tools for RNA-seq read counts. Genome Biol. 15, R29 (2014). [PubMed: 24485249]

61. Robinson MD & Oshlack A A scaling normalization method for differential expression analysis of RNA-seq data. Genome Biol. 11, R25 (2010). [PubMed: 20196867]

62. Dobin A et al. STAR: ultrafast universal RNA-seq aligner. Bioinformatics 29, 15–21 (2013). [PubMed: 23104886]

63. Robinson JT et al. Integrative genomics viewer. Nat. Biotechnol. 29, 24–26 (2011). [PubMed: 21221095]

64. Bindea G et al. ClueGO: a Cytoscape plug-in to decipher functionally grouped gene ontology and pathway annotation networks. Bioinformatics 25, 1091–1093 (2009). [PubMed: 19237447]

65. Szklarczyk D et al. STRINGv10: protein–protein interaction networks, integrated over the tree of life. Nucleic Acids Res. 43, D447–D452 (2015). [PubMed: 25352553]

66. Shannon P et al. Cytoscape: a software environment for integrated models of biomolecular interaction networks. Genome Res. 13, 2498–2504 (2003). [PubMed: 14597658]

67. Liu F, Song Y & Liu D Hydrodynamics-based transfection in animals by systemic administration of plasmid DNA. Gene Ther. 6, 1258–1266 (1999). [PubMed: 10455434]

68. Kozak M Primer extension analysis of eukaryotic ribosome-mRNA complexes. Nucleic Acids Res. 26, 4853–4859 (1998). [PubMed: 9776744]

69. Ran FA et al. Genome engineering using the CRISPR-Cas9 system. Nat. Protoc. 8, 2281–2308 (2013). [PubMed: 24157548]
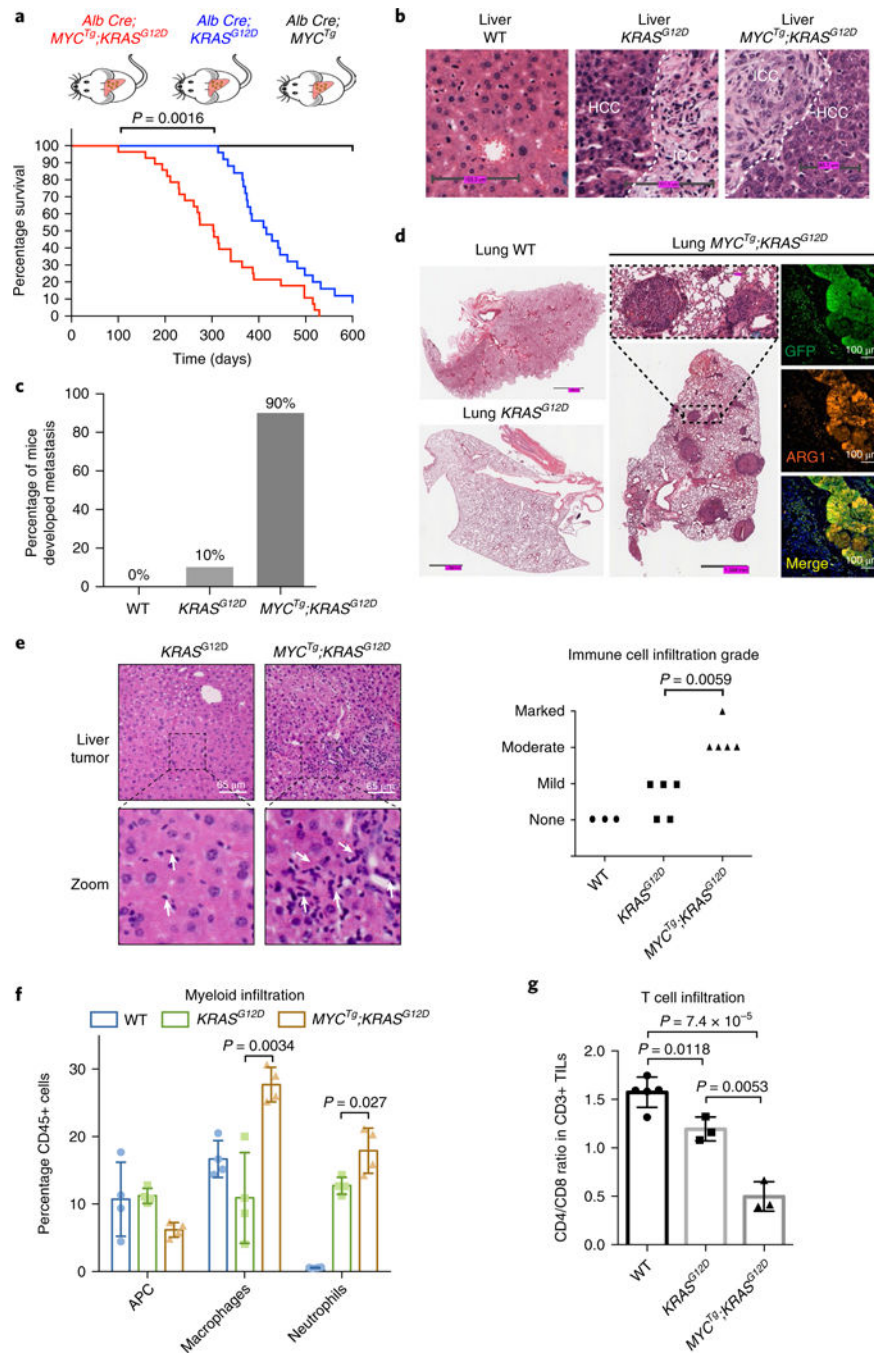
Fig. 1 |. *MYC* and *KRAS* cooperate to promote liver cancer with metastatic potential and induce marked alterations of immune populations compared with *KRAS* alone.
a, Kaplan–Meier curves showing tumor-free survival of $MYC^{Tg};KRAS^{G12D}$, $KRAS^{G12D}$, and MYC^{Tg} mice. $n = 22$ per genotype (log-rank test). **b**, Representative wild-type (WT), $KRAS^{G12D}$, or $MYC^{Tg};KRAS^{G12D}$ mice liver histology, $n = 3$ independent experiments is shown. ICC: intrahepatic cholangiocarcinoma (scale bars, WT: 103.3 μm, $KRAS^{G12D}$: 111.3 μm, $MYC^{Tg};KRAS^{G12D}$: 65.7 μm). **c**, Percentage of wild-type ($n = 3$) $KRAS^{G12D}$ ($n = 10$) or $MYC^{Tg};KRAS^{G12D}$ ($n = 10$) mice developed lung metastasis during cancer development.

d, Representative wild-type, $KRAS^{G12D}$ and MYC^{Tg};$KRAS^{G12D}$ mice lung histology, $n = 5$ independent experiments are shown. Immunofluorescence staining for GFP (indication of MYC overexpression), ARG1 (arginase-1, HCC marker, not expressed in the lung), and DAPI in MYC^{Tg};$KRAS^{G12D}$ lung section. **e**, Left: representative HCC histology in $KRAS^{G12D}$ and MYC^{Tg};$KRAS^{G12D}$ mice showing different grades of immune infiltration, $n = 3$ independent experiments (scale bars, 65 μm). White arrows represent inflammatory cell infiltration. Right: clinical evaluation of the grade of immune cells infiltration of the liver histology of wild-type ($n = 3$), $KRAS^{G12D}$ ($n = 5$), and MYC^{Tg};$KRAS^{G12D}$ ($n = 5$) mice (none: 0/HPF, mild: 1–3 per HPF, moderate 4–10 per HPF, marked >10 per HPF). Two-sided t test. **f**, Quantifications by flow cytometry of antigen-presenting cell (APC) (CD45+, CD11b–, CD11c +), macrophages (CD45 + , CD11b + , CD11c–, Ly6G/C–), and neutrophils (CD45+, CD11b+, CD11c–, Ly6G/C+) infiltrations into the liver tumors of wild-type, $KRAS^{G12D}$, or MYC^{Tg};$KRAS^{G12D}$ mice. $n = 4$. Two-sided t test. **g**, CD4/CD8 T cell ratio in wild-type liver ($n = 5$), $KRAS^{G12D}$ ($n = 3$), and MYC^{Tg};$KRAS^{G12D}$ ($n = 3$) mice liver tumors. Two-sided t test. TILs: tumor-infiltrating lymphocytes. All values represent the mean ± s.d.
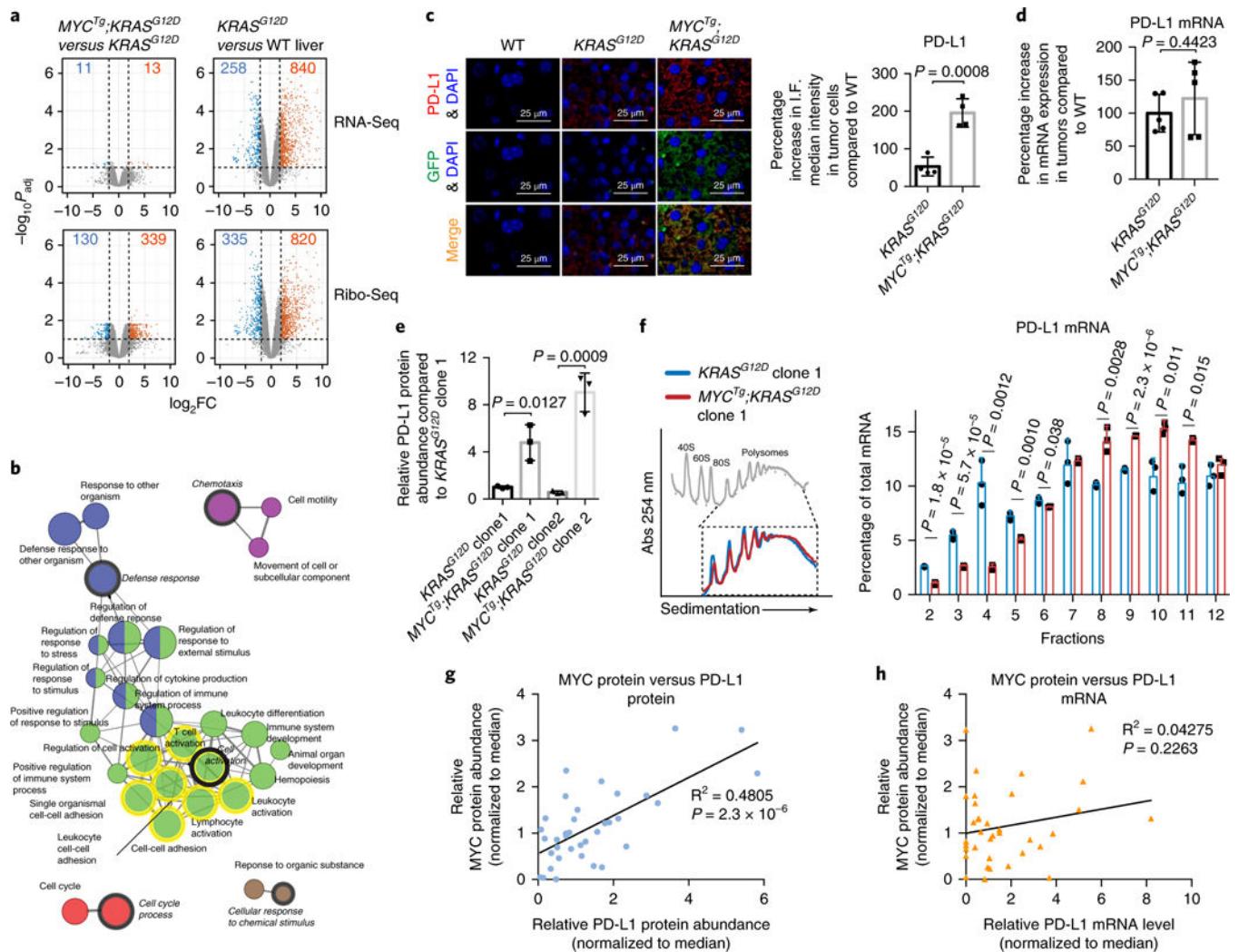
Fig. 2 |. A dichotomy in gene regulation between transcription versus translational control in $KRAS^{G12D}$ versus MYC^{Tg};$KRAS^{G12D}$ tumors.

a, Differential gene expression analysis shown as volcano plots, comparing MYC^{Tg};$KRAS^{G12D}$ ($n = 2$ animals) to $KRAS^{G12D}$ ($n = 2$ animals) (left panel), and comparing $KRAS^{G12D}$ ($n = 2$ animals) to wild type ($n = 3$ animals) (right panel) with RNA-Seq on the top and Ribo-Seq on the bottom. P values (two-sided t test) were adjusted using the Benjamini–Hochberg procedure for multi-testing. Dashed lines mark the threshold of significance in this study: the horizontal line marks the statistical significance ($P_{adj} < 0.1$) and the vertical lines mark the fold change (FC) ($|\log_2 FC| > 2$). The numbers of genes that pass this threshold are shown, with downregulated genes in blue and upregulated genes in orange. **b**, The network of enriched gene ontology categories (biological process) among 339 genes that are upregulated in Ribo-Seq comparing MYC^{Tg};$KRAS^{G12D}$ to $KRAS^{G12D}$ ($P_{adj} < 0.1$ and $\log_2 FC > 2$). The gene ontology network reflects the relationships between the gene ontology categories on the basis of the similarity of their associated genes, generated by ClueGO. Each node represents one enriched gene ontology category, with the size of the node representing the term enrichment significance (right-sided hypergeometric test). Edges indicate similarity (Kappa score > 0.4) between the two connected gene

ontology categories. Gene ontology categories are clustered into functional groups represented by different color codes. The mixed color coded nodes are shared between two functional groups. The most significantly enriched gene ontology category from each group is designated as the leading group term and highlighted in italics. The gene ontology terms that PD-L1 belongs to are highlighted in yellow circles. **c**, Left: representative PD-L1, GFP (indication of MYC overexpression) and DAPI immunofluorescence staining of wild-type mice livers, $KRAS^{G12D}$, or MYC^{Tg};$KRAS^{G12D}$ mice liver tumors (scale bars, 25 μm). Right: quantification of percentage increase in PD-L1 median intensity in $KRAS^{G12D}$ and MYC^{Tg};$KRAS^{G12D}$ tumor cells relative to the wild type. $n = 4$ independent experiments, two-sided t test. **d**, Percentage increase in PD-L1 mRNA expression levels in $KRAS^{G12D}$ or MYC^{Tg};$KRAS^{G12D}$ mice liver tumors relative to wild type, normalized to glyceraldehyde 3-phosphate dehydrogenase (GAPDH) mRNA. $n = 5$. **e**, Flow cytometry assessment of PD-L1 protein abundance in the $KRAS^{G12D}$ and MYC^{Tg};$KRAS^{G12D}$ HCC cell lines, $n = 3$ independent experiments, two-sided t test. **f**, Left: representative polysome trace of $KRAS^{G12D}$ and MYC^{Tg};$KRAS^{G12D}$ cell lines, $n = 3$ independent experiments. Inset highlights the polysomal fractions (7–12). Right: qualitative PCR with reverse transcription (RT-qPCR) analysis of PD-L1 mRNA levels in fractions, percentages of PD-L1 mRNA distributed in each fraction against total PD-L1 mRNA are shown. Two-sided t test. **g**, Comparison of relative MYC and PD-L1 protein abundance (normalized to median) in 36 fresh frozen human HCC patient samples by western blot. The 95% confidence interval for the Pearson coefficients is 0.4722–0.8322 (Pearson's correlation test, two-sided $P = 2.3 \times 10^{-6}$). **h**, Comparison of relative MYC protein abundance and relative PD-L1 mRNA expression (normalized to median) in 36 fresh frozen human HCC patient samples. The 95% confidence interval for the Pearson coefficients is –0.1307 to 0.5012 (Pearson's correlation test, two-sided $P = 0.2263$). All values represent the mean± s.d.
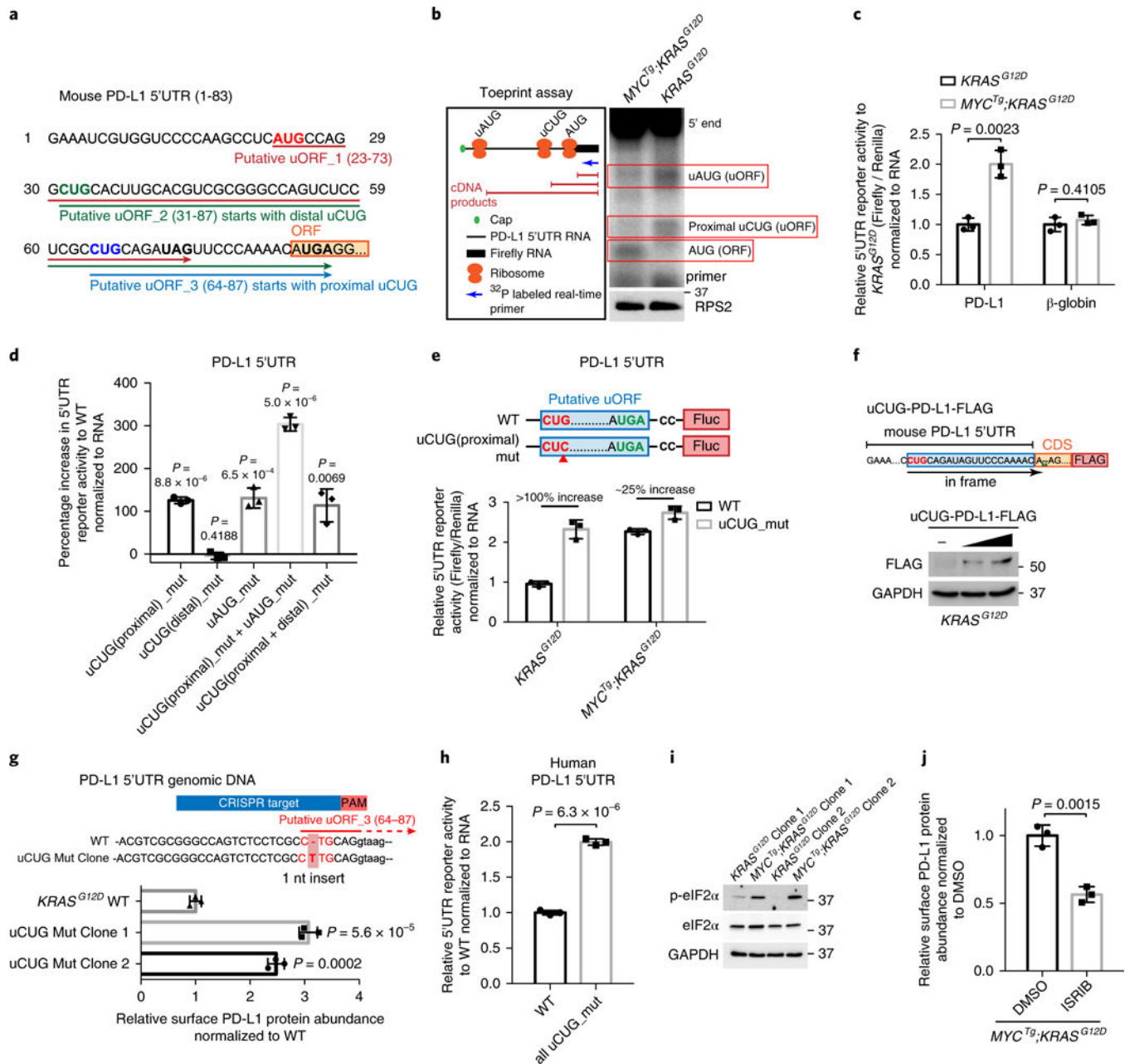
Fig. 3 |. PD-L1 expression is upregulated in MYC^{Tg};$KRAS^{G12D}$ cells through a bypass in uORF-mediated translational repression.

a, The sequence of the 5′UTR of mouse PD-L1 mRNA containing three putative uORFs initiating from uAUG, uCUG(distal), and uCUG(proximal), respectively. Stop codons for each putative uORF are in bold. **b**, Left: schematics of the toeprint assay. mRNAs composed of mouse PD-L1 5′UTR linked with firefly luciferase were used as the toeprint assay template. Right: autoradiography of the complementary DNA products from the toeprint assay using cytoplasmic lysate from $KRAS^{G12D}$ and MYC^{Tg};$KRAS^{G12D}$ cell lines. Red boxes highlight the bands indicating ribosome recognitions of the uAUG, uCUG(proximal), and AUG of the main ORF. RPS2 western blot is shown as controls for the amount of

ribosomes supplied in each reaction. **c**, 5′UTR reporter activity of mouse PD-L1 uORF-luciferase and β-globin 5′UTR luciferase (control) in $KRAS^{G12D}$ and MYC^{Tg};$KRAS^{G12D}$ cell lines. Two-sided t test, $n = 3$ independent experiments. **d**, Percentage increase in the 5′UTR reporter activity of mouse PD-L1 uORF-luciferase with point mutations (CU'G' to CU'C' or AU'G' to AU'C') in the three upstream start codons over that with wild type, in $KRAS^{G12D}$ cells. Two-sided t test, $n = 3$. **e**, 5′UTR reporter activity of mouse PD-L1 uORF-luciferase with and without a point mutation (CU'G' to CU'C') in the proximal uCUG start codon, in $KRAS^{G12D}$ and MYC^{Tg};$KRAS^{G12D}$ cells. $n = 3$ independent experiments. Percentages of increase (100% in $KRAS^{G12D}$ and 25% in MYC^{Tg};$KRAS^{G12D}$) in the luciferase activity of the uCUG mutation compared with wild type (WT) were shown. **f**, Upper: constructs for expressing a FLAG-tagged PD-L1 with 'AUG' start codon mutation (A'UGA' to A'A') (uCUG-PD-L1-FLAG). Lower: western blot of FLAG and GAPDH in $KRAS^{G12D}$ cell lines after 48-h transfection, $n = 3$ independent experiments. **g**, Upper: mouse PD-L1 5′UTR exon and intron DNA sequence of the wild-type (WT) and uCUG mutation $KRAS^{G12D}$ clonal cell line are shown. PAM region (AGG) is highlighted in red, which spans the 5′UTR exon and intron; CRISPR target region that against the 5′UTR exon is labeled in blue. 1 nucleotide (nt) insertion (CTG to C"T"TG) is detected in the uCUG start codon after the CRISPR/Cas9 editing. Lower: relative PD-L1 abundance in wild-type and two-mutation clonal cell lines determined by flow cytometry. Two-sided t test, $n = 3$ independent experiments. **h**, 5′UTR reporter activity of human PD-L1 uORF-luciferase with and without point mutations (CU'G' to CU'C') in the uCUG start codons in SNU-449 human HCC cell line (wild type, WT). Two-sided t test, $n = 3$ independent experiments. **i**, Western blot of p-eIF2α, eIF2α and GAPDH in $KRAS^{G12D}$ and MYC^{Tg};$KRAS^{G12D}$ cell lines. **j**, Relative PD-L1 protein abundance assessed by flow cytometry in MYC^{Tg};$KRAS^{G12D}$ cell lines treated with DMSO or 0.5 μM ISRIB for 72h. Two-sided t test, $n = 3$ independent experiments. All values represent the mean± s.d. Uncropped blots are provided in Supplementary Fig 15.
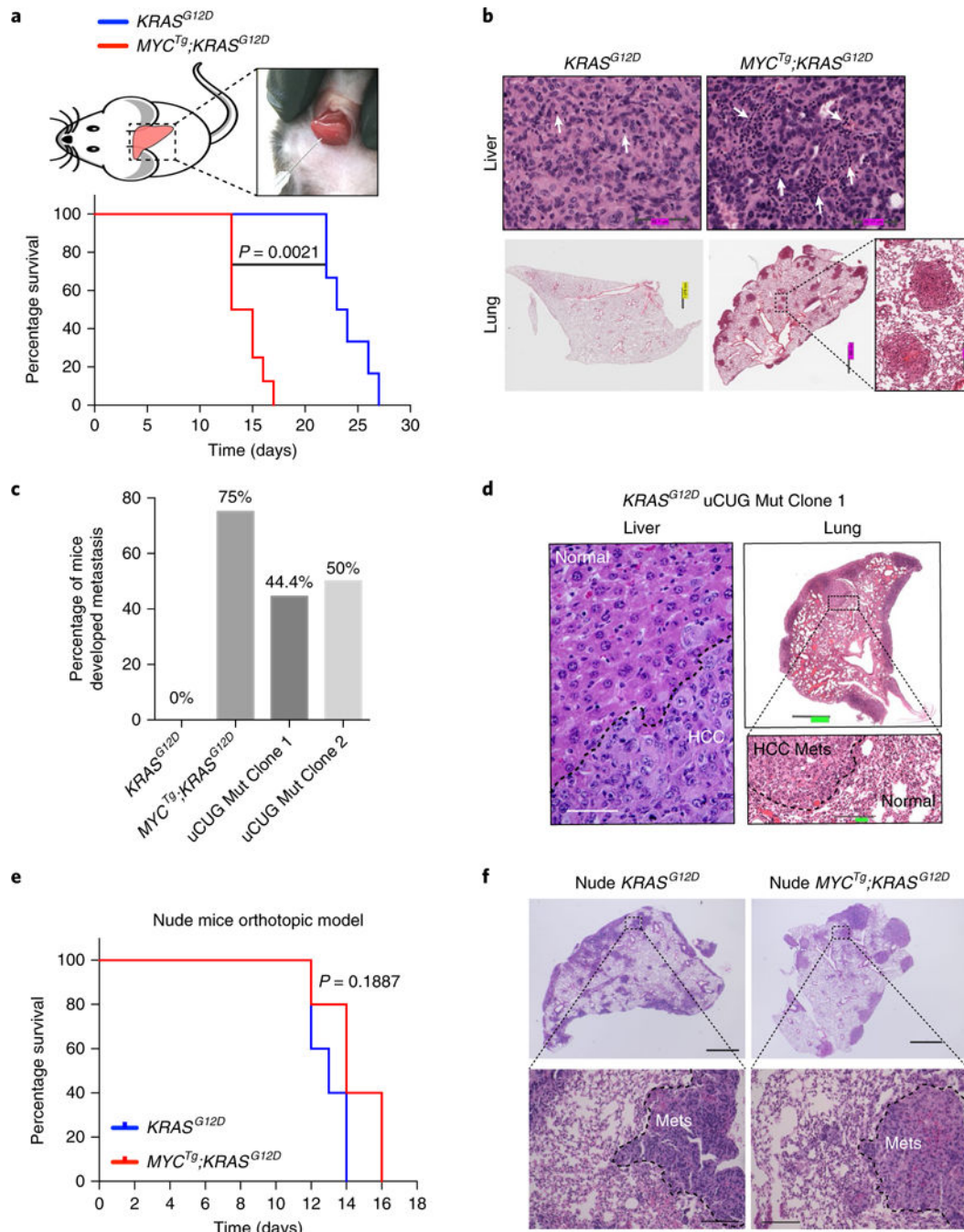
Fig. 4 |. The metastatic potential of MYC^{Tg};$KRAS^{G12D}$ tumors is dependent on PD-L1-mediated immune suppression.

a, Kaplan–Meier curves showing the survival of male C57/BL6 mice with $KRAS^{G12D}$ ($n = 6$) and MYC^{Tg};$KRAS^{G12D}$ ($n = 8$) cells orthotopically injected into livers. Wilcoxon rank sum test. **b**, Representative histology of livers and lungs of orthotopic $KRAS^{G12D}$ ($n = 5$) and MYC^{Tg};$KRAS^{G12D}$ ($n = 5$) C57BL/6 mice. White arrows represent inflammatory cell infiltration. **c**, Percentage of C57BL/6 mice injected with $KRAS^{G12D}$ ($n = 6$), MYC^{Tg};$KRAS^{G12D}$ ($n = 8$), $KRAS^{G12D}$ Mut Clone 1 ($n = 9$), or $KRAS^{G12D}$ Mut Clone 2 (n

= 8) cells developed metastasis. **d**, Representative histology of livers and lungs of orthotopic *KRAS*^{G12D} Mut Clone 1 mice ($n = 5$). Scale bars: left, 50 μm; upper right, 909.6 μm; lower right, 151.4 μm. **e**, Kaplan–Meier curves showing the survival of male athymic nude mice with *KRAS*^{G12D} ($n = 5$) and MYC^{Tg};*KRAS*^{G12D} ($n = 5$) cells orthotopically injected into the livers of nude mice. Wilcoxon rank sum test. **f**, Representative histology of lungs of orthotopic *KRAS*^{G12D} ($n = 5$) and *MYC*^{Tg};*KRAS*^{G12D} ($n = 5$) nude mice. Upper images: scale bar, 1,000 μm. Lower images: scale bar, 100 μm. Mets, metastases.
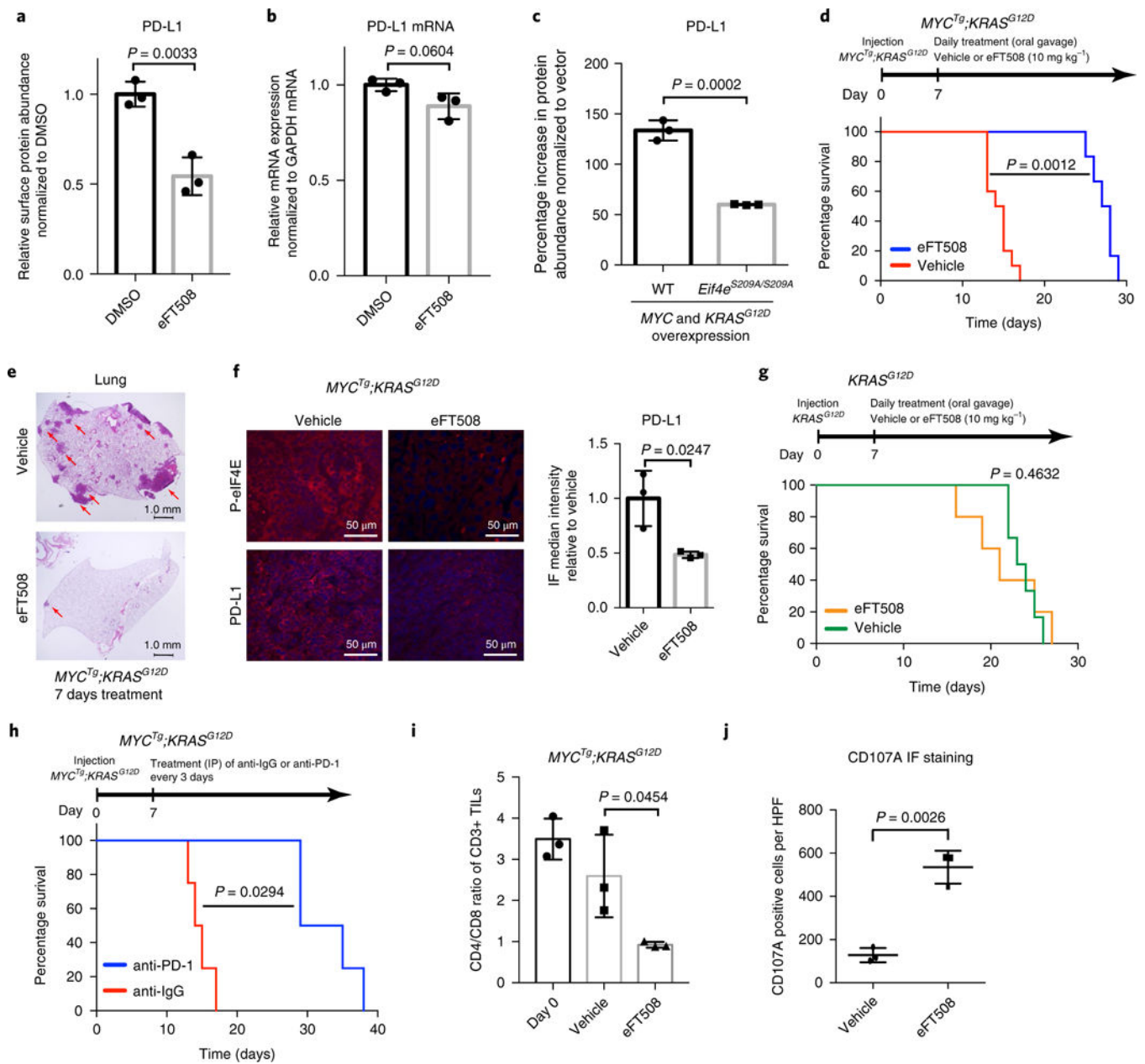
Fig. 5 |. p-eIF4E inhibition by eFT508 reduces PD-L1 abundance and prevents liver cancer progression and metastasis in vivo.

a, Relative surface PD-L1 abundance assessed by flow cytometry in MYC^{Tg};$KRAS^{G12D}$ cell lines treated with DMSO or 0.5 μM eFT508 for 72 h. $n = 3$ independent experiments, two-sided t test. **b**, Relative PD-L1 mRNA expression in $KRAS^{G12D}$ cell lines treated with DMSO or eFT508 for 48h. $n = 3$ independent experiments, two-sided t test. **c**, Percentage increase in the PD-L1 abundance in MYC and $KRAS^{G12D}$ overexpressed hepatocytes from wild type and $Eif4e^{S209A/S209A}$, compared with control vector transfected wild-type (WT) and Eif4e$^{S209A/S209A}$ hepatocyte, respectively, assessed by flow cytometry. $n = 3$ independent experiments, two-sided t test. **d**, Kaplan–Meier curves showing the survival of male C57/B6 mice with MYC^{Tg};$KRAS^{G12D}$ cells orthotopically injected into the livers.

Vehicle ($n = 10$ animals) or eFT508 (10 mg kg^{-1}) ($n = 6$ animals) was orally administered once a day starting 7 d post-tumor implantation. Wilcoxon rank sum test. **e**, Representative histology of lungs of MYC^{Tg};$KRAS^{G12D}$ injected mice after 7 d vehicle or eFT508 treatments (scale bars, 1.0 mm). Red arrows present metastases in the lungs. $n = 5$ animals. **f**, Immunofluorescence staining (IF) for p-eIF4E, PD-L1, and DAPI in MYC^{Tg};$KRAS^{G12D}$ liver section on 7d vehicle or eFT508 treatments, $n = 3$ independent experiments, two-sided t test (scale bars, 50 μm). **g**, Kaplan–Meier curves showing the survival of male C57/B6 mice with $KRAS^{G12D}$ cells orthotopically injected into the livers. Vehicle ($n = 6$ animals) or eFT508 (10 mgkg^{-1}) ($n = 5$ animals) was orally administered once a day starting 7 d post tumor implantation. Wilcoxon rank sum test. **h**, Kaplan–Meier curves showing the survival of male C57/B6 mice with MYC^{Tg};$KRAS^{G12D}$ cells orthotopically injected into the livers. Monoclonal antibodies against IgG ($n = 4$ animals) or PD-1 (200 μg per mouse) ($n = 4$ animals) were administered by intraperitoneal (IP) injection every 3 d starting 7 d post-implantation. Wilcoxon rank sum test. **i**, CD4/CD8 T cell ratio in the livers of mice injected with MYC^{Tg};$KRAS^{G12D}$ cells on 7-d vehicle ($n = 3$ animals) or eFT508 ($n = 3$ animals) treatment. Two-sided t test. **j**, Quantification of CD107A immunofluorescence intensity in MYC^{Tg};$KRAS^{G12D}$ liver section on 7-d vehicle ($n = 3$ animals) or eFT508 ($n = 3$ animals) treatments. Two-sided t test. All values represent the mean± s.d.